Tuning chirality amplitude at ultrafast timescales in chiral $CsCuCl_3$

Hiroki Ueda [1,*] Takahiro Sato [2] Quynh L. Nguyen,[2] Elizabeth Skoropata,[1] Ludmila Leroy,[1] Tim Suter,[3] Elsa Abreu [3] Matteo Savoini,[3] Vincent Esposito [2] Matthias Hoffmann [2] Carl P. Romao [4,5] Julien Zaccaro [6] Diling Zhu,[2] Steven Lee Johnson [1,3] and Urs Staub [1,†]

[1]*Center for Photon Science, Paul Scherrer Institute, 5232 Villigen-PSI, Switzerland*
[2]*Linac Coherent Light Source, SLAC National Accelerator Laboratory, Menlo Park, California, USA*
[3]*Institute for Quantum Electronics, Physics Department, ETH Zurich, 8093 Zurich, Switzerland*
[4]*Department of Materials, ETH Zurich, 8093 Zurich, Switzerland*
[5]*Department of Materials, Faculty of Nuclear Sciences and Physical Engineering, Czech Technical University in Prague, Trojanova 13, 120 00 Prague, Czech Republic*
[6]*Grenoble Alpes University, CNRS, Grenoble INP, Institut Néel, BP166, 38042 Grenoble Cedex 09, France*

(Received 20 May 2025; accepted 9 September 2025; published 14 October 2025)

Chirality is a fundamental symmetry concept relevant to many scientific fields. It describes discrete states, i.e., left-handed, right-handed, or achiral. In contrast to this discrete classification, objects can be continuously distorted. To describe the deviation from an achiral state, the chirality amplitude has to be addressed, similarly to magnetization being the "amplitude" for time-reversal symmetry breaking. Even though symmetry breaking is the base for many phenomena in science in general, symmetry cannot quantitatively predict measurable quantities. Chirality amplitude is the key quantity for quantifying chirality-related emergent phenomena. Here, we propose two types of chiral lattice distortions and report their ultrafast dynamics. We determine the ultrafast reduction of the chirality amplitude in $CsCuCl_3$ after an optical excitation by using resonant x-ray diffraction with circular polarization. An additional symmetry breaking representing a nonhanded chiral structure is observed by resonant x-ray diffraction when exciting the material with an intense, low-cycle terahertz pulse. The latter demonstrates a hidden enantiomorphic pair in a nonhanded chiral structure. The concept of chirality amplitude, as well as the decomposition into two different types of chiral lattice distortions, suggests a unique approach toward controlling chirality-induced emergent phenomena.

DOI: 10.1103/36tg-vr5k

I. INTRODUCTION

Chirality is a universal concept for defining the handedness of an object and is relevant in widely spread scientific communities, such as biology, chemistry, and particle physics. In condensed matter physics, it has become a lively topic, e.g., chiral magnetism [1], chiral fermions [2], and chiral phonons [3], which lead to emergent phenomena, such as chiral edge states [4], nonreciprocal transport [5], and phonomagnetism [6–8]. Although chirality is a basic symmetry concept underlying these phenomena, the role of a related order parameter is not well addressed compared to other symmetry concepts, despite a substantial number of reported emergent phenomena based on this symmetry concept [9–12]. For example, magnetization acts as a well-established order parameter for time-reversal symmetry breaking. One can define chirality amplitude in a crystal lattice as the lattice distortion associated with chiral symmetry breaking, representing the structural deviation from the centrosymmetric space group. Hence, a measurement of the structural distortion contains a direct relation to the development of chirality as an order parameter, i.e., the chirality amplitude. The onset of chirality breaks all roto-inversion symmetries, but a ferroic order parameter with a switchable conjugate field remains missing. The absence of such a conjugate field makes it challenging to control chiral states with a few exceptions where a chiral-achiral phase transition accompanies another ferroic order, e.g., ferroelectricity [13–16] or ferroelasticity [17].

In the fields of chemistry and biochemistry, the importance of chirality amplitude, quantified by the so-called continuous chirality measure [18], has indeed been discussed in asymmetric catalysis and structure-activity correlations of bioreceptors [19,20], and also plays a role in particle physics [21]. Given that chirality is an essential ingredient of various emergent phenomena in condensed matter systems, tuning the *static* crystal chirality amplitude, e.g., by chemical substitution [22], is the most straightforward and intuitive approach to manipulate resulting phenomena, e.g., optical rotatory. As an asymmetric lattice distortion is often responsible for emergent spin and orbital textures [23–25], enhancing or reducing the chirality amplitude [see Fig. 1(b)] can unbalance competing interactions. Yet largely unexplored is the *dynamics* of the crystal chirality amplitude.

*Contact author: hiroki.ueda@psi.ch
†Contact author: urs.staub@psi.ch

Published by the American Physical Society under the terms of the Creative Commons Attribution 4.0 International license. Further distribution of this work must maintain attribution to the author(s) and the published article's title, journal citation, and DOI.

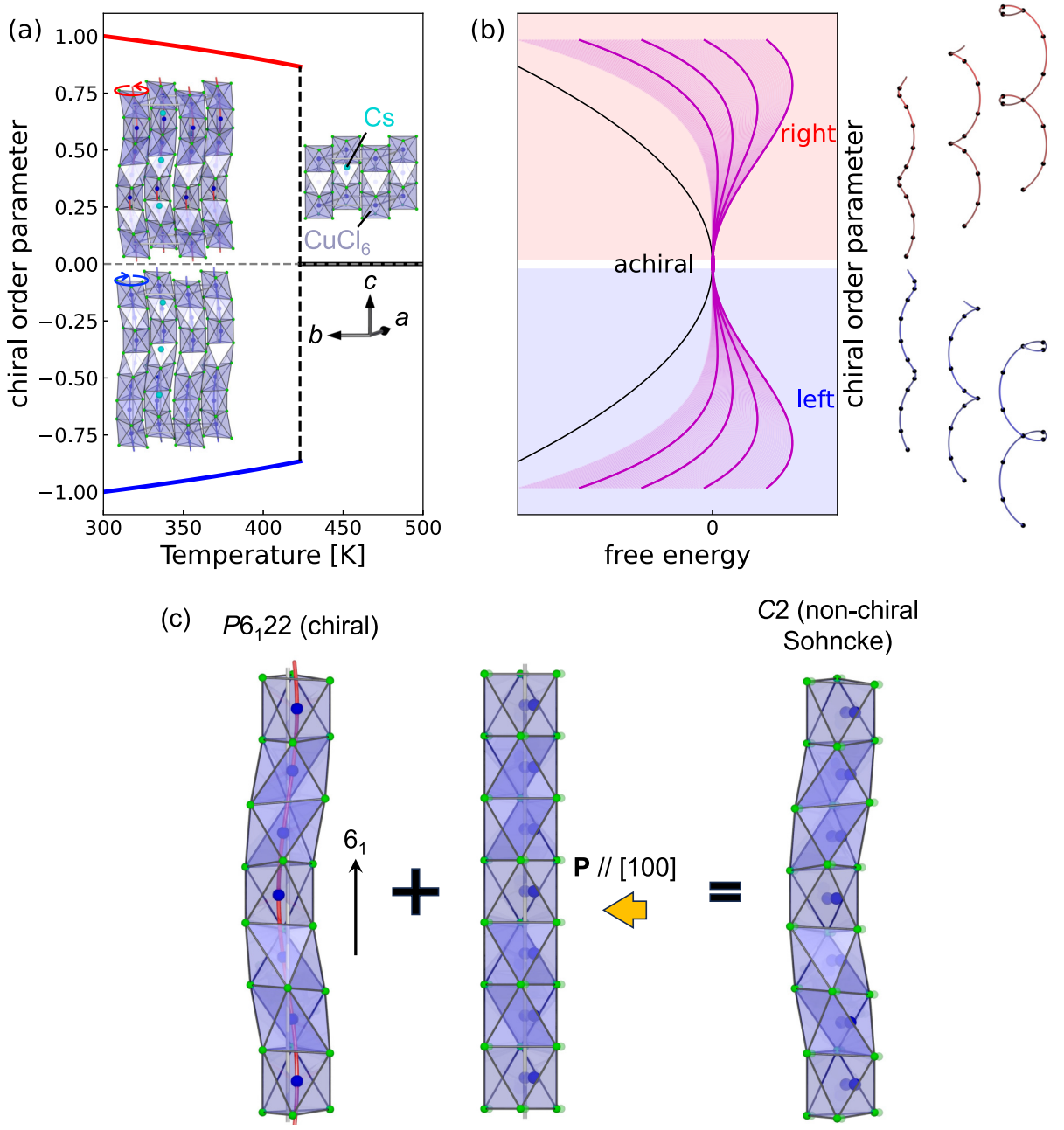


FIG. 1. (a) Temperature dependence of the order parameter for the chiral phase transition in $CsCuCl_3$, i.e., an e-p chiral order parameter. Insets show corresponding crystal structures. Data are extracted from Ref. [28]. The order parameter is normalized to the value at 300 K. The sign of the order parameter corresponds to chirality, either left-handed (negative, blue) or right-handed (positive, red). (b) The concept of the chiral order parameter. Chirality is either there (chiral, double-well potential) or not (achiral, either single-well potential or double-well potential with thermal fluctuation). If existing, it defines the handedness, either left or right, which is an e-p chiral order parameter. However, one can continuously distort the structure to make the chirality amplitude smaller or larger, as visualized by red and blue helices with different chirality amplitude on the right. (c) An example of e-u chiral lattice distortions. The development of an in-plane polarity along the twofold rotation axis in a structure with space group $P6_122$ reduces the symmetry and results in a structure with space group $C2$, which is one of the nonchiral Sohncke groups with nonhanded chirality. Here, we extract only a part of the crystal structure for simplicity.

$CsCuCl_3$ is an excellent candidate to tackle this issue as it exhibits a phase transition from the centrosymmetric ($P6_3/mmc$) to the chiral phases with an enantiomorphic pair (e-p) [$P6_522$ (left-handed) or $P6_122$ (right-handed)] at $T_C = 423\,\mathrm{K}$, as seen in Fig. 1(a), allowing us to quantify chirality amplitude as structural distortion from the centrosymmetric phase. The transition is purely gyrotropic, meaning no onset of any trivial ferroic order, e.g., ferroelectricity or ferroelasticity, preventing the trivial control of chirality via an external stimulus [26]. Multiple techniques have manifested its chiral coordination below T_C by, e.g., optical rotation [27], x-ray and neutron diffraction [28], and, most directly, resonant x-ray diffraction with circular polarization [29,30]. The superlattice reflection intensities and the

TABLE I. Two types of chiral lattice distortions, classified by characterizing space groups.

Distortion type	Space group
e-p	Tetragonal: $P4_1$-$P4_3$, $P4_122$-$P4_322$, $P4_12_12$-$P4_32_12$ Trigonal: $P3_1$-$P3_2$, $P3_112$-$P3_212$, $P3_121$-$P3_221$ Hexagonal: $P6_1$-$P6_5$, $P6_2$-$P6_4$, $P6_122$-$P6_522$, $P6_222$-$P6_422$ Cubic: $P4_132$-$P4_332$
e-u	Triclinic: $P1$ Monoclinic: $P2$, $P2_1$, $C2$ Orthorhombic: $P222$, $P222_1$, $P2_12_12$, $P2_12_12_1$, $C222_1$, $C222$, $F222$, $I222$, $I2_12_12_1$ Tetragonal: $P4$, $P4_2$, $I4$, $I4_1$, $P422$, $P42_12$, $P4_222$, $P4_22_12$, $I422$, $I4_122$ Trigonal: $P3$, $R3$, $P312$, $P321$, $R32$ Hexagonal: $P6$, $P6_3$, $P622$, $P6_322$ Cubic: $P23$, $F23$, $I23$, $P2_13$, $I2_13$, $P432$, $P4_232$, $F432$, $F4_132$, $I432$, $I4_132$

circular contrast in a forbidden reflection peak intensity of resonant x-ray diffraction directly measure the chirality amplitude as a structural deviation from the centrosymmetric phase. Figure 1(a) represents the temperature dependence of the chiral order parameter extracted by taking the square root of x-ray or neutron diffraction intensities of a superlattice reflection peak originating from the phase transition and optical rotatory power, shown in Ref. [28].

We propose two types of chiral lattice distortions that characterize a general chiral structure and their dynamics at ultrafast timescales. One type relates to an e-p of space groups, and the other type does not have an e-p, i.e., a nonhanded chiral structure. We refer to the latter type of lattice distortions as an enantiomorphic unpair (e-u) chiral lattice distortion. One may see that the first type describes distortions characterizing the 22 chiral space groups, while the second type describes those characterizing of the rest of the Sohncke groups [31] (see Table I for the overview and Appendix A for details). When a chiral lattice distortion describes a phase transition, the distortion is a chiral order parameter with either e-p or e-u character.

To probe the chirality amplitude, we employ resonant x-ray diffraction with circular polarization that can directly determine the handedness [32] and measure the chirality amplitude. By extending this technique into the time domain, we investigate the ultrafast dynamics of chirality amplitude in the chiral crystal $CsCuCl_3$, triggered by an optical (400 nm) or terahertz (THz) pulse. An e-p chiral lattice distortion is the order parameter of a chiral-achiral phase transition and, thus, belongs to the A_1 symmetry. An optical excitation can drive a fully symmetric mode, e.g., via the displacive excitation mechanism, and/or create a thermal effect, which follows the symmetry of the lattice. Therefore, it can directly modulate the e-p chiral lattice distortion [see Fig. 1(b)], offering an ideal platform to investigate its dynamics. A THz excitation can directly drive an IR-active mode, which breaks the symmetry of a nonpolar chiral state. Depending on which symmetry

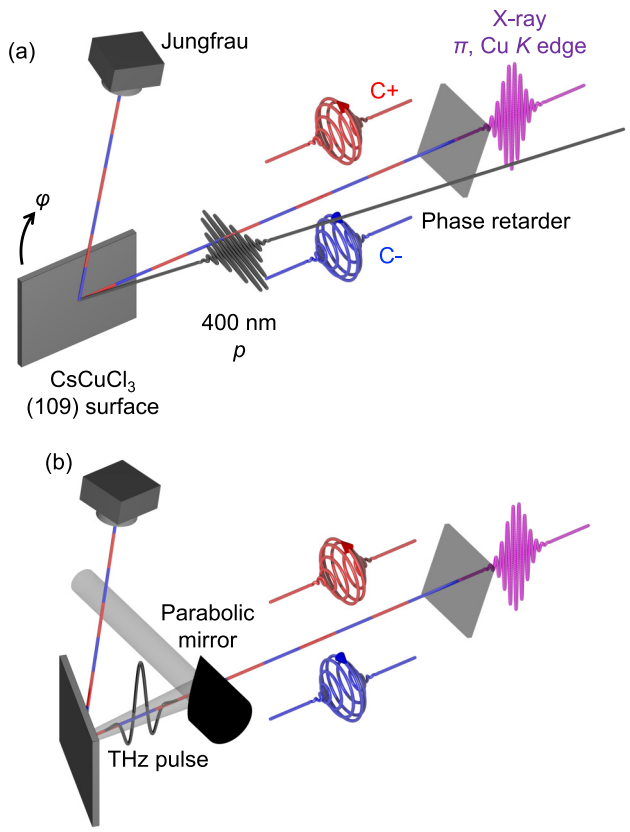


FIG. 2. Experimental setups of pump-probe resonant x-ray diffraction with circularly polarized x-rays: (a) optical pump and (b) THz pump. For the optical pump setup, pump (gray) and probe (red, blue, or pink, depending on polarization) beams are noncollinear with a grazing incidence angle of 0.5° to the sample surface for x-rays in order to minimize the penetration depths mismatch. For the THz pump setup, the two beams are collinear and the incidence angle is relatively large between 40° and 70°. A diamond-based phase retarder converts x-ray polarization from vertical (π, purple) to circular [C+ (red) or C–(blue)]. The sample is rocked along the surface normal (ϕ) at a fixed incidence angle.

to break, the resultant structure can become another chiral state nominally without an e-p. Such THz-induced lattice distortions are e-u chiral. Figure 1(c) shows a case where an in-plane polar distortion in a chiral structure characterized by space group $P6_122$ results in $C2$ symmetry, which belongs to a nonchiral Sohncke group. Although it is a nonhanded chiral structure, this symmetry consideration indicates that a nonchiral Sohncke group can be characterized by both e-p and e-u chiral lattice distortions. The proposed ultrafast approaches can test the concept of two types of chiral lattice distortions.

II. RESULTS AND DISCUSSION

We performed time-resolved resonant x-ray diffraction experiments with circularly polarized x-ray pulses on an enantiopure $CsCuCl_3$ single crystal at ambient conditions (see Fig. 2 for the two experimental setups and Appendix B for details). The x-ray photon energy was tuned in the vicinity of the Cu K edge ($1s \rightarrow 4p$) based on the x-ray absorption

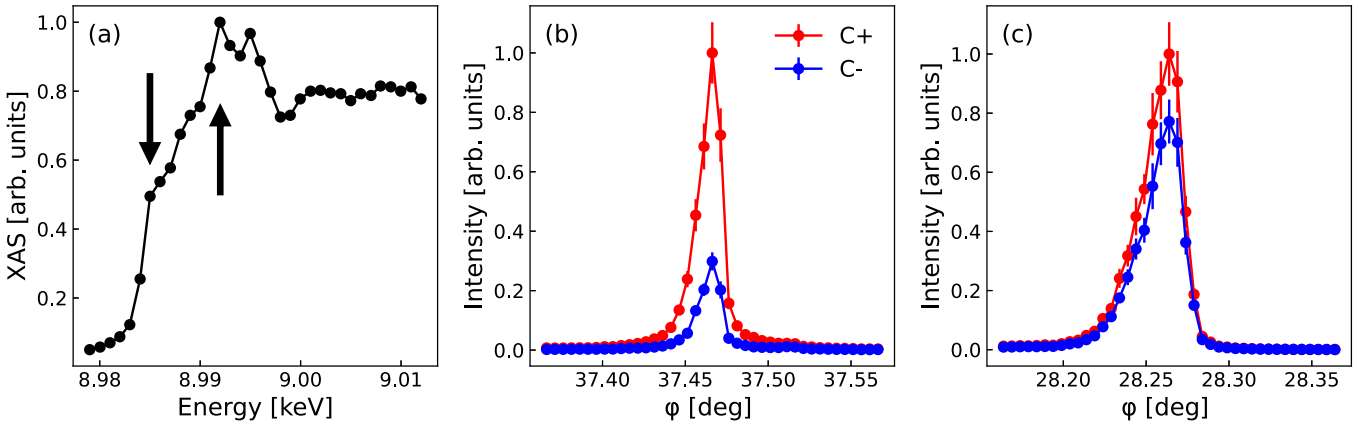


FIG. 3. (a) XAS around the Cu K edge. The black arrows represent the photon energies employed for the diffraction measurements [8.985 keV for the (0 0 10) reflection and 8.992 keV for the (1 0 20) reflection]. Rocking curves with circular polarization around (b) the (0 0 10) forbidden reflection and (c) the (1 0 20) allowed reflection. Error bars are standard errors.

spectrum (XAS), shown in Fig. 3(a). At these photon energies, the resonant x-ray scattering process has additional sensitivity to the Cu^{2+} $4p$ states, which form a chiral arrangement in the chiral structure of $CsCuCl_3$.

For the optical pump experiments, we focused on the (0 0 10) space-group forbidden reflection due to its direct sensitivity to crystal chirality, as manifested by the circular contrast in its intensity shown in Fig. 3(b) and also in Ref. [29]. As described in Appendix C and Ref. [30], the (0 0 10) forbidden reflection arises purely from electric quadrupole (orbital) scattering and has circular-polarization-dependent diffraction intensities described as

$$I^{P_2}_{(0\,0\,10)} = \tfrac{27}{8}|\langle Q_{x^2-y^2}\rangle|^2(1+\sin^2\theta)(1+\chi P_2 \sin\theta)^2, \quad (1)$$

$$I^{+1}_{(0\,0\,10)} - I^{-1}_{(0\,0\,10)} \propto \chi|\langle Q_{x^2-y^2}\rangle|^2. \quad (2)$$

Here, θ is the Bragg angle, P_2 ($=\pm1$ for C+ and C− circular polarizations) denotes the circular polarization state of an incident x-ray beam, χ represents crystal chirality [±1 for right- and left-handedness; see Fig. 1(a)], and $Q_{x^2-y^2}$ is a local Cu^{2+} $4p$ electric quadrupole moment with x being along the twofold axis $\langle 110\rangle$ of the site and y being normal to both x and [001] (z). The circular contrast in the diffraction intensities is proportional to chirality χ and the square of the expectation value of the electric quadrupole moment $\langle Q_{x^2-y^2}\rangle$, which becomes zero in the centrosymmetric phase and describes the chiral-achiral phase transition. Namely, the amplitude of circular contrast measures the amplitude of the e-p chiral order parameter $|\langle Q_{x^2-y^2}\rangle|$, and the sign of the circular contrast defines the handedness of the chiral crystal structure. The circular contrast does not depend on the incidence angle but on the Bragg angle, which is fixed for the given x-ray energy at resonance [see Eq. (C6) in Appendix C]. Note that this resonantly allowed space-group forbidden reflection in the chiral phase becomes forbidden, even at resonance, once the crystal transforms to the centrosymmetric phase. An e-p chiral lattice distortion does not change the symmetry of the chiral space group but continuously varies chirality amplitude with defined handedness, e.g., the one shown in Fig. 1(b). This type of mode belongs to the totally symmetric irreducible representation A_1, but it is noteworthy that not all A_1 modes are e-p chiral.

For the THz pump experiments, we additionally measured the (1 0 20) space-group allowed Bragg reflection, which also shows a circular contrast at resonance, as shown in Fig. 3(c). The (1 0 20) reflection appears as an allowed superlattice reflection only below the chiral phase transition. Therefore, this reflection intensity measures the structural distortion from the centrosymmetric phase (charge scattering), in particular Cu^{2+} (the Wyckoff position $2a$) motions, in addition to $\langle Q_{x^2-y^2}\rangle$ and $\langle Q_{3z^2-r^2}\rangle$ of the Cu^{2+} $4p$ electric quadrupole moments, which resonantly contributes to the diffraction intensities and may give rise to the interference effect with the charge scattering [33]. Note that, in general, the circular contrast requires finite intensities in the polarization rotation channel, i.e., $\sigma-\pi$' and/or $\pi-\sigma$'. This means that the orbital scattering contributions must be involved to obtain a circular contrast because charge scattering is isotropic and cannot create x-ray polarization rotations by itself. However, the existence of an interference term between the orbital and charge scatterings can transfer changes in the charge scattering amplitude, including the onset of an e-u chiral lattice distortion, into changes in circular contrast even without an electric quadrupole modulation (e.g., e-p chiral order parameter). Symmetry lowering can create e-u type of chiral structure. In this regard, chirality amplitude enhancement can also be achieved by further symmetry reduction, corresponding to the onset of an e-u chiral lattice distortion. A model case is a phase transition from one of the chiral space groups to one of the nonchiral Sohncke groups, as an example illustrated in Fig. 1(c).

A. Optical excitation

Figure 4(a) shows time traces of the (0 0 10) reflection intensity with both circular x-ray polarizations following the above bandgap optical excitation ($\sim$30 mJ/cm^2) [34]. In addition to the clear intensity reduction in each polarization channel, the circular contrast also decreases. The circular contrast is directly proportional to the square of the expectation value of the electric quadrupole moment [see Eq. (2)],

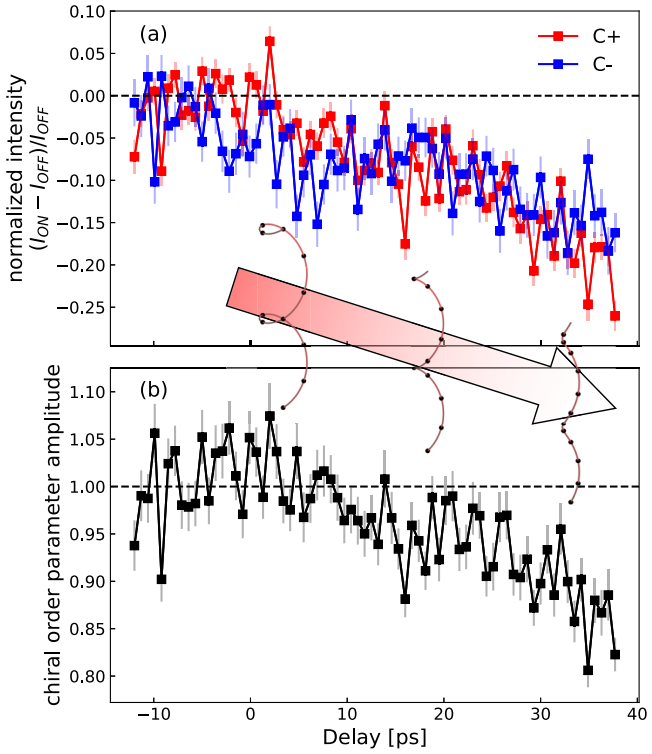


FIG. 4. Time trace of the chiral order parameter following the optical excitation. (a) Normalized intensity $(I_{ON}–I_{OFF})/I_{OFF}$ for the (0 0 10) forbidden reflection with two polarization C+ (red) and C– (blue) and (b) the e-p chiral order parameter obtained by taking the square root of the circular contrast signal $(I_{C+}–I_{C–})_{ON}/(I_{C+}–I_{C–})_{OFF}$. The origin of the horizontal axis is when pump and probe beams temporary overlap on the sample. Error bars are standard errors.

which represents here the e-p chiral order parameter. This reduction implies that the chirality amplitude has decreased by ∼13% in the probed region at 38 ps after the optical excitation. The comparison to the equilibrium case of the e-p chiral order parameter shown in Fig. 1(a) allows us to assign an average temperature of the probed region that almost reaches T_C at ∼38 ps after the photoexcitation. Since there is a relatively large mismatch in the penetration depths between the pump (∼26 nm) and probe (∼138 nm) beams [35,36] even at the grazing incidence, most of the energy is deposited at the surface and dissipates into deeper-lying regions on slower timescales. This interpretation is consistent with a thermal effect and the observed slow dynamics of the e-p chiral order parameter shown in Fig. 4(b). The deposited energy density at the surface is much higher than that needed to bring the sample above T_C, which transforms the surface to the centrosymmetric phase, as found in Fig. 1(a). In the recovery process to the low-temperature chiral phase, the crystal chooses between one of the handedness (left- or right-handed). The absence of any clear change in diffraction intensity for both circular polarization channels over the repetition of the data acquisition indicates that the recovery process deterministically chooses the original chiral state. This is most likely due to the fact that the remaining deeper-lying region of the crystal acts like a seed, in contrast to the case of the thermal cycle, where chiral nucleation with random handedness leads to a racemic state [28].

B. THz excitation

The blue plot in Fig. 5(a) represents the transmitted THz intensity spectrum through a thin $CsCuCl_3$ crystal (∼500 μm) measured by THz time-domain spectroscopy (see Appendix D for details). The employed geometry is sensitive to IR-active phonon modes with in-plane polarity, i.e., doubly degenerate E_1 modes. The strong absorption around 2–2.5 THz is consistent with the previously reported E_1 modes [37], whose frequencies are highlighted by light-red bars and tabulated in Table II in Appendix E. The presence of the E_1 modes in this frequency range is supported by our density functional perturbation theory (DFPT) calculations (see Table III in Appendix F). The black curve in Fig. 5(a) shows the fast Fourier transform spectrum of the THz electric field measured by electro-optic sampling (EOS) and used to drive IR-active modes in the time-resolved resonant x-ray diffraction experiment. The spectral range matches well some doubly degenerate E_1 (light-red bars) and nondegenerate IR-active A_2 (light-blue bars) phonon modes.

A mode directly modifying the e-p chiral order parameter must belong to the totally symmetric irreducible representation A_1. The (0 0 10) reflection is directly sensitive to the e-p order parameter modifications, but there is no detectable variation of its intensity following a THz pulse (see Fig. 7). Therefore, the e-p chiral order parameter does not strongly couple to the THz pulse resonant to the IR-active phonons. Note that the penetration depths are comparable between pump and probe beams, and the deposited energy density is approximately 4 orders of magnitude less compared to the optical pump, which excludes thermal effects observed in the optical excitation case (see Appendix B for details).

Figures 5(c) and 5(d) show the time traces of the (1 0 20) Bragg reflection intensity with opposite circular polarizations and the corresponding circular contrast, respectively. The THz pulse evidently modulates the diffraction intensities. Their fast Fourier transform spectra, plotted in Fig. 5(b), show multiple peaks. The prominent peaks are close to the IR-active A_2 mode(s) at ∼1.5 THz and the IR-active E_1 modes at ∼2 and ∼2.5 THz [37]. These polar eigenmodes break the equilibrium nonpolar symmetry of $P6_{1(5)}22$. Especially, an E_1 mode possesses developed electric polarization in the basal plane, meaning the onset of e-u chiral lattice distortions due to symmetry breaking [see Fig. 1(c)].

The peak amplitude in the fast Fourier transform spectra might exhibit certain dichroism [see, for example, the peaks at ∼1.5 and ∼2 THz in Fig. 5(b)]. This can be explained when the orbital scattering terms and/or the pure charge scattering that interferes with the orbital scattering show modulations. Both cases could result in the observed circular contrast in the fast Fourier transform spectra. Note that in equilibrium, the (1 0 20) reflection has an additional sensitivity to $\langle Q_{3z^2-r^2}\rangle$ than the (0 0 10) reflection, which is solely sensitive to $\langle Q_{x^2-y^2}\rangle$.

When a polar lattice distortion occurs in a nonpolar chiral structure, a snapshot (within a cycle of the oscillation frequency) of the resultant crystal structure is polar and chiral

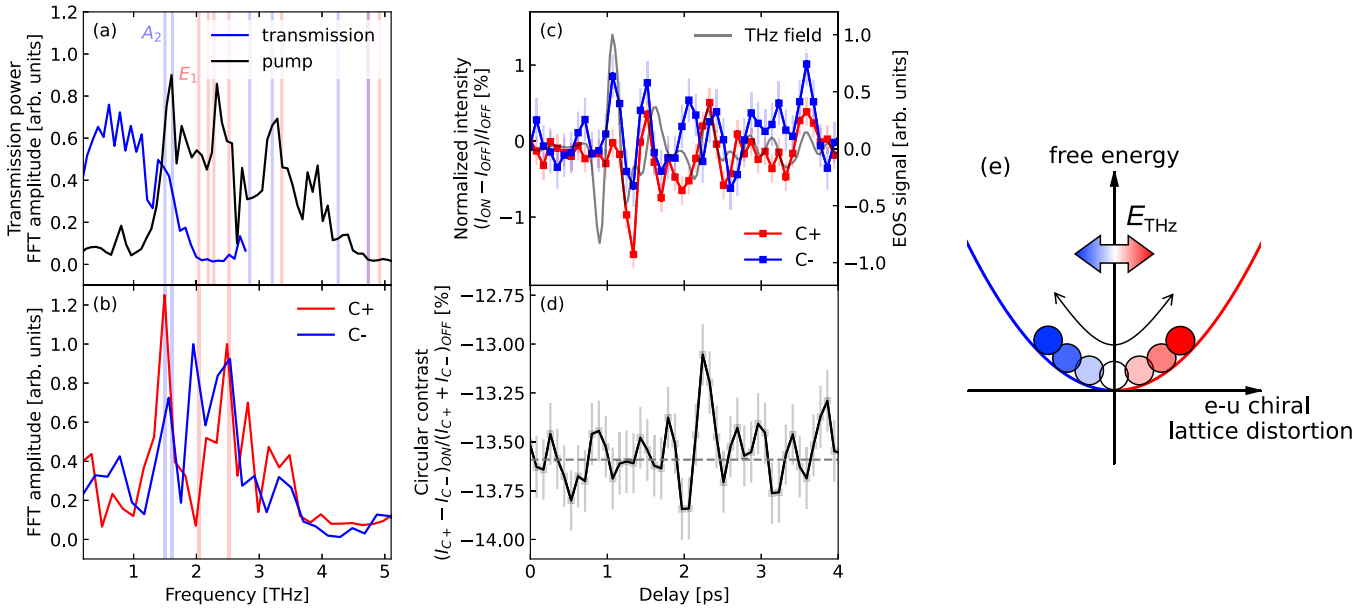


FIG. 5. | (a) THz spectra of transmission power (blue) and electric field used as a pump beam in the time-resolved resonant x-ray diffraction experiment (black). Light-color bars represent IR-active A_2 (blue) or E_1 (red) phonon modes reported in Ref. [37]. (b) Fast Fourier transform spectra of the time traces of the (1 0 20) reflection intensities [red (C+) and blue (C−)]. Selected relevant A_2 (blue) and E_1 (red) phonon frequencies are represented by light-color bars as panel (a). Time traces of the diffraction intensities of the (1 0 20) allowed reflection with circular polarization: (c) normalized intensities $(I_{ON}–I_{OFF})/I_{OFF}$ for C+ and C–, and (d) corresponding circular contrast. Gray curve in panel (c) represents the time trace of a THz electric field of the pump. Error bars are standard errors. (e) A schematic of the emerged e-u chiral lattice distortion oscillating around the equilibrium triggered by a THz electric field.

simultaneously, compatible with the parent space group and the broken symmetry. Therefore, the character of the resultant space group depends on the direction of polarity. Note that the symmetry remains the same in the time average. For the case of $CsCuCl_3$ with the space group $P6_{1(5)}22$, the maximum polar subgroups of $P6_{1(5)}22$ are $P6_{1(5)}$ for an out-of-plane moment (A_2) and $C2$ for an in-plane moment (E_1). While $P6_{1(5)}$ belongs to a chiral space group, $C2$ does not belong to a chiral space group but to a Sohncke group. Such space groups have been recognized to exhibit only nonhanded chiral states [38]. However, this symmetry argument based on our time-resolved

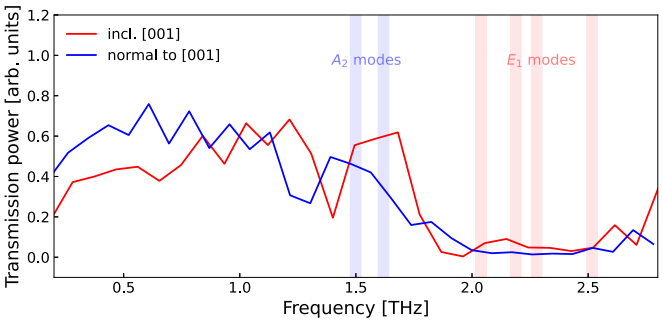


FIG. 6. THz spectra of transmission power through a $CsCuCl_3$ slab crystal with a (109) surface. Red with a THz electric field maximized [001] projection and blue without [001] component of a THz electric field. Light-color bars represent IR-active A_2 (light blue) or E_1 (light red) phonon modes reported in Ref. [37]. The THz electric field was rotated to maximize the [001] component during the time-resolved resonant x-ray diffraction experiment, and thus, the blue plot is just for comparison.

study suggests that the latter can be characterized by both e-p and e-u chiral lattice distortions [see Fig. 1(c)], depending on how the symmetry in the parent phase is broken. The coherent E_1 phonon excitation oscillates the amplitude as well as the sign of the e-u chiral lattice distortions, as schematically illustrated in Fig. 5(e). Beyond this symmetry argument, which can also be deduced from the IR spectroscopy, the technique employed here, in principle, allows us to quantify the e-p and e-u chiral lattice distortions. In this study, however, the simultaneous multiple phonon excitations prevent us from achieving it.

The deconvolution of a chiral structure belonging to a nonchiral Sohncke group into e-p and e-u chiral lattice distortions can be generalized also in equilibrium. It might allow to assign emergent functionalities to the "handedness" in a nonhanded chiral structure as the two types of chiral lattice distortions likely affect differently chirality-related phenomena. Identifying the key distortions helps in understanding emergent phenomena and designing materials. Very recently, the induction of macroscopic chirality in a nonchiral crystal possessing compensated chiral sublattices with opposite handedness, namely, an antiferro-chiral state, has been reported based on nonlinear phononic coupling, i.e., driving an IR-active mode coupling to a Raman-active mode that lifts off the degeneracy of two chiral sublattices and results in a nonchiral Sohncke group [39,40]. This clearly suggests the existence of an e-p chiral lattice distortion in a nonchiral Sohncke group.

Directly tuning interactions associated with a chiral lattice distortion by coherently exciting specific phonon modes, e.g., electromagnons [41,42] and chiral soft phonons [43], may also provide a platform to investigate the role of chirality

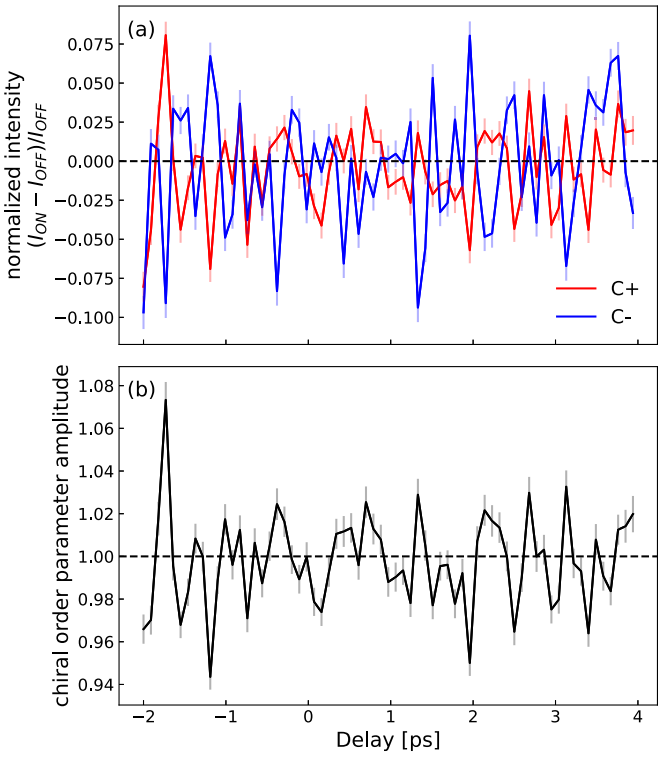


FIG. 7. Time trace of the e-p chiral order parameter following the THz excitation. (a) Normalized intensity $(I_{ON}–I_{OFF})/I_{OFF}$ for the (0 0 10) forbidden reflection with two polarization C+ (red) and C− (blue), and (b) the e-p chiral order parameter obtained by taking the square root of the circular contrast signal $(I_{C+}–I_{C-})_{ON}/(I_{C+}–I_{C-})_{OFF}$. The origin of the horizontal axis is when pump and probe beams temporary overlap on the sample. Error bars are standard errors.

amplitude in physics. An intense THz pulse has the potential for macroscopic emergence or coherent excitation of the chirality degree in a phononic system. In relation to being developed "chiral" phononics [3,6–8,44], the concept of chirality amplitude and the decomposition of a nonhanded chiral structure into two distinct types of chiral lattice distortions may be keys toward further exploration of chirality-related emergent phenomena.

ACKNOWLEDGMENTS

We acknowledge M. Suzuki from Kwansei Gakuin University for his help in developing the diamond-based phase retarder. We thank S.-W. Huang and B. Pedrini for their support of static sample characterization. The time-resolved x-ray diffraction experiments were carried out at the XPP beamline in the Linac Coherent Light Source (LCLS), SLAC National Accelerator Laboratory. Use of LCLS is supported by the U.S. Department of Energy, Office of Science, Office of Basic Energy Sciences under Contact No. DE-AC02-76SF00515. H.U. was partially supported by the National Centers of Competence in Research in Molecular Ultrafast Science and Technology (NCCR MUST-No. 51NF40-183615) from the Swiss National Science Foundation and from the European Union's Horizon 2020 research and innovation program under the Marie Skłodowska-Curie Grant Agreement No. 801459—FP-RESOMUS. Q.L.N. acknowledges support from the Bloch Fellowship in Quantum Science and Engineering by the Stanford-SLAC Quantum Fundamentals, Architectures, and Machines Initiative. E.S. received funding from the European Union's Horizon 2020 research and innovation program under the Marie Skłodowska-Curie Grant Agreement No. 884104 (PSI-FELLOW-III-3i). C.P.R. acknowledges support from the project FerrMion of the Ministry of Education, Youth and Sports, Czech Republic, co-funded by the European Union (CZ.02.01.01/00/22_008/0004591), the European Union and Horizon 2020 through Grant No. 10103035, and ETH Zurich. Computational resources were provided by the Swiss National Supercomputing Center (CSCS) under project ID eth3.

DATA AVAILABILITY

The data that support the findings of this article are openly available [45]; embargo periods may apply.

APPENDIX A: SOHNCKE GROUPS

Chiral crystal structures, belonging to the so-called Sohncke groups, have space groups that contain only symmetry operations of the first kind, i.e., rotations, roto-translations, and translations. Note that not all chiral crystal structures belong to chiral space groups [31]. Among 65 Sohncke groups, 22 groups are chiral and have enantiomorphic pairs of space groups reflecting opposite chirality, e.g., $P3_121$-$P3_221$ and $P6_122$-$P6_522$ (see Table I). For the remaining 43 groups, e.g., $P312$ and $P432$, a roto-inversion operation relates them to themselves. As a result, these groups are achiral, and there are no distinct space groups for enantiomers with opposite handedness, though the crystal structure is chiral. We call a crystal structure belonging to this type an e-u chiral state. Asymmetry found in these types of Sohncke groups appears to be nonhanded chiral [38].

APPENDIX B: TIME-RESOLVED RESONANT X-RAY DIFFRACTION

We performed time-resolved resonant x-ray diffraction experiments with circularly polarized x-ray pulses on an enantiopure $CsCuCl_3$ single crystal at ambient conditions at the XPP beamline in the Linac Coherent Light Source, SLAC National Accelerator Laboratory in the USA. Figure 2(a) shows the experimental setup for the optical pump part. The optical pump beam is p-polarized 400 nm (3.1 eV) with a pulse duration of 50 fs, while the bandgap of $CsCuCl_3$ is ∼2.6 eV [35]. The employed fluence was 30 mJ/cm^2. Using the monochromator based on the diamond (1 1 1) configuration, x-ray photon energy was tuned in the vicinity of the Cu K edge ($1s \rightarrow 4p$) with a bandwidth of 0.6–0.7 eV and a pulse duration of 30−40 fs. The photon energy was calibrated by the x-ray absorption spectrum measured in the fluorescence mode from the sample [see Fig. 3(a)]. The mechanically polished (1 0 9) surface allows us to employ a grazing incidence angle of 0.5° at the Bragg condition for the (0 0 10) forbidden reflection, and the pump beam is noncollinear to the probe beam with a relative angle of ∼7°. These conditions reduce the penetration depth

mismatch between the x-ray probe and the optical pump. The probe depth is ∼138 nm [36], whereas the pump penetration depth is ∼26 nm [35]. A Jungfrau pixel detector simultaneously collected x-ray diffraction and fluorescence signals. A diamond-based phase retarder converts x-ray polarization from linear to circular by detuning the diamond crystal angle from the (2 2 0) Laue geometry and switching between two offset angles by a piezo actuator [46]. The thickness of the diamond crystal is 960 μm. The measured sample was the same enantiopure $CsCuCl_3$ crystal as in the previous resonant soft x-ray diffraction study [30]. Figure 2(b) shows the experimental setup for the THz pump part. We generated a THz pulse via the optical rectification of a near-infrared pulse in a DSTMS (4-*N*,*N*-dimethylamino-4′-*N*′-methyl-stilbazolium 2,4,6-trimethylbenzenesulfonate) crystal [47]. The peak field strength measured by EOS was ∼500 kV/cm at the sample position after focusing the beam with a 3 inch effective focal length parabolic mirror. The THz beam path from the generation part to the sample was purged with dry air to avoid atmospheric water vapor absorption. The incidence angles for the (1 0 20) allowed reflection and the (0 0 10) forbidden reflection are ∼70° and ∼40°, respectively. These relatively large incidence angles guarantee a large THz electric field strength on the sample. The corresponding fluences were 0.28 and 0.19 mJ/cm^2 for the incidence angles of 70° and 40°, respectively. The penetration depths of the pump and probe beams are ∼7.5 and ∼13.5 μm, respectively, at an incidence angle of 70° and ∼5.1 and ∼9.2 μm, respectively, at an incidence angle of 40°.

APPENDIX C: RESONANT X-RAY DIFFRACTION INTENSITIES

Let us formulate the chirality-dependent diffraction intensities of the (0 0 10) forbidden reflection at the Cu *K* edge [30]. The x-ray scattering at atomic resonance is sensitive to x-ray polarization, and an x-ray susceptibility tensor is

$$\hat{f} = \begin{pmatrix} f_{xx} & f_{xy} & f_{zx} \\ f_{xy} & f_{yy} & f_{yz} \\ f_{zx} & f_{yz} & f_{zz} \end{pmatrix}. \tag{C1}$$

We take the local Cartesian coordinate *xyz*, where *x* is along the twofold axis ⟨110⟩ of the Cu site, *z* is along [001], and *y* is normal to both directions. Each tensor component has a relation to the expectation value of an electric quadrupole moment as $\langle Q_{xy}\rangle = \frac{2}{\sqrt{3}} f_{xy}$, $\langle Q_{zx}\rangle = \frac{2}{\sqrt{3}} f_{zx}$, $\langle Q_{yz}\rangle = \frac{2}{\sqrt{3}} f_{yz}$, $\langle Q_{x^2-y^2}\rangle = \frac{1}{\sqrt{3}}(f_{xx} - f_{yy})$, and $\langle Q_{3z^2-r^2}\rangle = \frac{1}{2}(2f_{zz} - f_{xx} - f_{yy})$ [48]. The trace component corresponds to electric monopole (charge) scattering. The local C_2 symmetry along *x* requires a relation $\hat{f} = C_2 \hat{f} C_2^{-1}$. This results in $f_{xy} = f_{zx} = 0$, i.e.,

$$\hat{f} = \begin{pmatrix} f_{xx} & 0 & 0 \\ 0 & f_{yy} & f_{yz} \\ 0 & f_{yz} & f_{zz} \end{pmatrix}. \tag{C2}$$

The sixfold screw symmetry along *z* connects each Cu^{2+} position with the Wyckoff position of 6*a*. The form factor of the (*h k l*) resonant diffraction at the Cu *K* edge is given by summing up the x-ray scattering susceptibility together with a phase factor over all Cu^{2+} contributing to the scattering:

$$\begin{aligned} \hat{F}_{(hkl)} = N\big[& \hat{f} e^{2\pi i h x} + C_6^{\chi} \hat{f} C_6^{-\chi} e^{2\pi i (hx + kx + l/6)} \\ & + C_6^{2\chi} \hat{f} C_6^{-2\chi} e^{2\pi i (kx + l/3)} + C_6^{3\chi} \hat{f} C_6^{-3\chi} e^{2\pi i (-hx + l/2)} \\ & + C_6^{4\chi} \hat{f} C_6^{-4\chi} e^{2\pi i (-hx - kx + 2l/3)} \\ & + C_6^{5\chi} \hat{f} C_6^{-5\chi} e^{2\pi i (-kx + 5l/6)} \big]. \end{aligned} \tag{C3}$$

Here, $x = 0.0616$ is the atomic coordinate of the Cu^{2+} site [49], χ is the chirality of a crystal structure [+1 for right-handed ($P6_122$) and −1 for left-handed ($P6_522$)], and *N* is the number of unit cells contributing to the scattering.

Only Cu^{2+} 4*p* electric quadrupoles (orbital asphericity) can contribute to the structurally forbidden (0 0 10) reflection. When using circular polarization for incident x-rays with the Stokes parameter P_2 (+1 and −1 for C+ and C−, respectively), we can obtain diffraction intensities with circular polarization dependence by using the following general expression of diffraction intensity:

$$\begin{aligned} I_{(h\,k\,l)} = {} & \tfrac{1}{2}\big(\big|\hat{F}^{\sigma'\sigma}_{(h\,k\,l)}\big|^2 + \big|\hat{F}^{\pi'\sigma}_{(h\,k\,l)}\big|^2 + \big|\hat{F}^{\sigma'\pi}_{(h\,k\,l)}\big|^2 + \big|\hat{F}^{\pi'\pi}_{(h\,k\,l)}\big|^2 \big) \\ & + P_2 \mathrm{Im}\big(\hat{F}^{\sigma'\pi}_{(h\,k\,l)}{}^{*} \hat{F}^{\sigma'\sigma}_{(h\,k\,l)} + \hat{F}^{\pi'\pi}_{(h\,k\,l)}{}^{*} \hat{F}^{\pi'\sigma}_{(h\,k\,l)} \big). \end{aligned} \tag{C4}$$

For $(h\,k\,l) = (0\,0\,10)$, the circular contrast is proportional to chirality χ as well as the square of the expectation value of the electric quadrupole $\langle Q_{x^2-y^2}\rangle$,

$$I^{P_2}_{(0\,0\,10)} = \tfrac{27}{8} |\langle Q_{x^2-y^2}\rangle|^2 (1 + \sin^2\theta)(1 + \chi P_2 \sin\theta)^2, \tag{C5}$$

$$I^{P_2=1}_{(0\,0\,10)} - I^{P_2=-1}_{(0\,0\,10)} = \tfrac{27}{2} \chi |\langle Q_{x^2-y^2}\rangle|^2 \sin\theta (1 + \sin^2\theta), \tag{C6}$$

where θ is the Bragg angle. The circular contrast directly measures chirality amplitude $|\langle Q_{x^2-y^2}\rangle|$. Unlike trigonal crystals [32], the diffraction intensity formulated as Eq. (1) is independent of the azimuthal angle along [001]. This is because the azimuthal angle dependence in trigonal crystals appears through the interference of scatterings by two electric quadrupole moments, while there is only the single electric quadrupole moment contributing to the (0 0 10) diffraction intensity in the hexagonal $CsCuCl_3$.

For $(h\,k\,l) = (1\,0\,20)$, electric monopoles of Cu^{2+}, which sit on the Wyckoff position 6*a*, and two Cu^{2+} 4*p* electric quadrupoles, $\langle Q_{x^2-y^2}\rangle$ and $\langle Q_{3z^2-r^2}\rangle$, contribute to the diffraction intensities and can give rise to circular contrast as the (0 0 10) reflection via the orbital scattering or its interference effect with the charge scattering [33].

APPENDIX D: THZ TIME-DOMAIN SPECTROSCOPY

THz time-domain spectroscopy using an OH1 [2-(3-(4-hydroxystyryl)-5,5-dimethylcyclohex-2-enylidene)malononitrile)] crystal [50] to generate a THz pulse was performed on a thin (∼500 μm thickness) crystal with a polished (109) surface. Figure 6 shows the transmission power of a THz beam. For this measurement, we used two geometries where the THz electric field has the largest [001] component (red) or is normal to [001] (blue). Thus, both geometries pick up an IR-active mode with in-plane polarity, i.e., an E_1 mode. The strong absorption around 2–2.5 THz observed for both spectra is consistent with the previously reported doubly degenerate E_1 phonon modes [37].

TABLE II. Phonons in the chiral phase of $CsCuCl_3$ from IR and Raman spectroscopies. Frequency and irreducible representation (Irrep.) were taken from Ref. [37]. LO and TO represent a longitudinal optical mode and a transverse optical mode, respectively. An A_2 mode is IR-active with polarity along [001], whereas an E_1 mode is IR-active with polarity in the basal plane. These IR-active modes were measured at 300 K, whereas the Raman-active A_1 and E_2 modes were measured at 326 and 341 K, respectively.

Freq. (THz)	Irrep.	Freq. (THz)	Irrep.
0.52	A_2 (TO)	3.21	A_2 (LO)
0.53	A_2 (LO)	3.36	E_1 (TO)
0.72	E_2	3.42	E_1 (LO)
0.82	A_1	3.96	E_2
1.29	E_2	4.26	A_2 (TO)
1.50	A_2 (TO)	4.65	E_2
1.59	E_2	4.74	E_1 (TO)
1.62	A_2 (LO)	4.74	A_2 (LO)
1.80	E_2	4.92	E_1 (LO)
1.99	E_2	5.35	A_1
2.04	E_1 (TO)	5.43	A_2 (TO)
2.19	E_1 (LO)	5.52	A_2 (LO)
2.28	E_1 (TO)	5.82	E_2
2.52	E_1 (LO)	7.28	E_2
2.55	E_2	7.94	A_2 (TO)
2.85	A_2 (TO)	8.63	A_1
3.07	A_1	8.66	A_2 (LO)

APPENDIX E: PHONON FREQUENCIES FROM PREVIOUS STUDY

Table II summarizes phonon modes in the chiral phase of $CsCuCl_3$, excerpted from Ref. [37].

APPENDIX F: DFPT CALCULATIONS

DFPT calculations of the phonon frequencies of $CsCuCl_3$ in the chiral phase were performed using the abinit software package (version 9) [51]. The calculations were performed using the projector augmented wave (PAW) method with the local-density approximation exchange-correlation functional. PAW basis sets were used as received from the abinit library. A plane-wave basis set cutoff energy of 130 Ha inside the PAW spheres and 26 Ha outside, and a $4 \times 4 \times 4$ Monkhorst-Pack grid [52] of **k**-points were chosen for the calculations following convergence studies. The Hubbard U correction, in combination with an antiferromagnetic arrangement of magnetic moments of the Cu atoms (alternating along the chains), was found to be necessary to open a band gap and thereby correctly model $CsCuCl_3$ as a band insulator with LO-TO splitting. The Hubbard U parameters $U = 15$ eV and $J = 1$ eV were chosen as the minimum magnitude of U-J that opened a band gap (4.2 eV). Prior to the phonon calculation, the structure was relaxed to an internal pressure of 10 MPa. The resulting calculated Γ point phonon frequencies are shown in Table III, and a JSON file with their eigenvectors, which can be visualized using phonon website [53], is available as supplemental data. An input file for the DFPT calculation and the output derivative database are also available [45].

TABLE III. Phonons in the chiral phase of $CsCuCl_3$ from DFPT calculations. Frequency at the Γ point and irreducible representation (Irrep.), obtained by DFPT calculations, are shown. Acoustic modes are not shown.

Freq. (THz)	Irrep.	Freq. (THz)	Irrep.	Freq. (THz)	Irrep.	Freq. (THz)	Irrep.
0.688	E_2 (TO)	2.33	E_1 (TO)	4.19	E_1 (TO)	5.84	E_1 (TO)
0.688	E_2 (LO)	2.35	E_1 (LO)	4.21	E_1 (LO)	5.95	E_1 (LO)
0.824	A_1 (TO)	2.51	A_2 (LO)	4.22	A_2 (LO)	7.08	B_1 (TO)
1.11	E_1 (TO)	2.51	B_1 (TO)	4.38	B_2 (TO)	7.25	E_2 (TO)
1.12	E_1 (LO)	2.59	A_2 (LO)	4.61	E_2 (TO)	7.25	E_2 (LO)
1.16	B_2 (TO)	2.64	E_1 (TO)	4.61	E_2 (LO)	7.39	A_1 (LO)
1.28	B_1 (TO)	2.75	E_1 (LO)	4.67	E_1 (TO)	7.64	E_1 (TO)
1.30	A_2 (LO)	2.80	E_1 (TO)	4.79	E_1 (LO)	7.68	E_1 (LO)
1.31	E_2 (LO)	2.80	E_1 (LO)	4.91	B_1 (TO)	7.71	B_1 (TO)
1.31	E_2 (TO)	2.88	E_2 (TO)	5.07	B_1 (TO)	7.90	E_2 (TO)
1.39	E_1 (TO)	2.88	E_2 (LO)	5.08	E_2 (TO)	7.90	E_2 (LO)
1.40	E_1 (LO)	3.08	E_1 (TO)	5.08	E_2 (LO)	8.03	A_1 (TO)
1.57	B_1 (TO)	3.09	E_1 (LO)	5.16	E_1 (TO)	8.16	E_1 (TO)
1.63	E_2 (TO)	3.13	E_2 (TO)	5.30	A_1 (TO)	8.29	A_1 (TO)
1.63	E_2 (LO)	3.13	E_2 (LO)	5.31	E_2 (TO)	8.42	E_1 (LO)
1.90	A_2 (TO)	3.57	E_2 (TO)	5.31	E_2 (LO)	8.59	E_1 (TO)
1.99	E_1 (TO)	3.57	E_2 (LO)	5.40	B_2 (TO)	8.90	E_1 (LO)
2.01	E_1 (LO)	3.70	A_1 (TO)	5.44	E_1 (LO)	8.93	E_2 (TO)
2.11	B_2 (TO)	3.76	B_1 (TO)	5.52	A_2 (LO)	8.93	E_2 (LO)
2.18	E_2 (TO)	3.83	E_2 (TO)	5.56	B_2 (TO)	9.12	B_2 (TO)
2.18	E_2 (LO)	3.83	E_2 (LO)	5.61	E_2 (TO)		
2.19	A_1 (TO)	3.92	B_2 (TO)	5.61	E_2 (LO)		

APPENDIX G: TIME TRACE OF THE (0 0 10) FORBIDDEN REFLECTION FOLLOWING THZ EXCITATION

Figure 7 represents the time traces of the (0 0 10) forbidden reflection intensities following the THz pulse. Unlike the (1 0 20) allowed reflection intensities shown in Fig. 5(c), the (0 0 10) reflection did not show any clear dynamics within our experimental precision. This result shows that the THz pulse does not significantly affect the Cu^{2+} $4p$ electric quadrupoles $\langle Q_{x^2-y^2} \rangle$.

[1] S.-W. Cheong and X. Xu, Magnetic chirality, npj Quantum Mater. **7**, 40 (2022).

[2] M. Zahid Hasan, G. Chang, I. Belopolski, G. Bian, S.-Y. Xu, and J.-X. Yin, Weyl, Dirac and high-fold chiral fermions in topological quantum matter, Nat. Rev. Mater. **6**, 784 (2021).

[3] H. Ueda, M. García-Fernandez, S. Agrestini, C. P. Romao, J. van den Brink, N. A. Spaldin, K.-J. Zhou, and U. Staub, Chiral

phonons in quartz probed by X-rays, Nature (London) **618**, 946 (2023).
[4] M. König, S. Wiedmann, C. Brüne, A. Roth, H. Buhmann, L. W. Molenkamp, X.-L. Qi, and S.-C. Zhang, Quantum spin Hall insulator state in HgTe quantum wells, Science **318**, 766 (2007).
[5] R. Aoki, Y. Kousaka, and Y. Togawa, Anomalous nonreciprocal electrical transport on chiral magnetic order, Phys. Rev. Lett. **122**, 057206 (2019).
[6] J. Luo, T. Lin, J. Zhang, E. R. Blackert, R. Xu, B. I. Yakobson, and H. Zhu, Large effective magnetic fields from chiral phonons in rare-earth halides, Science **382**, 698 (2023).
[7] M. Basini, M. Pancaldi, B. Wehinger, M. Udina, V. Unikandanunni, M. C. Hoffmann, A. V. Balatsky, and S. Bonetti, Terahertz electric-field-driven dynamical multiferroicity in $SrTiO_3$, Nature (London) **628**, 534 (2024).
[8] C. S. Davies, F. G. N. Fennema, A. Tsukamoto, I. Razdolski, A. V. Kimel, and A. Kirilyuk, Phononic switching of magnetization by the ultrafast Barnett effect, Nature (London) **628**, 540 (2024).
[9] Y. Tokura, S. Seki, and N. Nagaosa, Multiferroics of spin origin, Rep. Prog. Phys. **77**, 076501 (2014).
[10] A. Fert, N. Reyren, and V. Cros, Magnetic skyrmions: Advances in physics and potential applications, Nat. Rev. Mater. **2**, 17031 (2017).
[11] J. Mun, M. Kim, Y. Yang, T. Badloe, J. Ni, Y. Chen, C.-W. Qiu, and J. Rho, Electromagnetic chirality: From fundamentals to nontraditional chiroptical phenomena, Light: Sci. Appl. **9**, 139 (2020).
[12] T. Wang, H. Sun, X. Li, and L. Zhang, Chiral phonons: Prediction, verification, and application, Nano Lett. **24**, 4311 (2024).
[13] H. Iwasaki, K. Sugii, N. Niizeki, and H. Toyoda, Switching of optical rotatory power in ferroelectric $5PbO{\cdot}3GeO_2$ single crystal, Ferroelectric **3**, 157 (1972).
[14] J. Kobayashi, K. Uchino, H. Matsuyama, and K. Saito, Optical study on domain switching of ferroelectric triglycine sulfuric acid and Rochelle salt, J. Appl. Phys. **69**, 409 (1991).
[15] R. Matsuda, Y. Kaneko, Y. Tokura, and Y. Takahashi, Electric field control of natural optical activity in a multiferroic helimagnet, Science **372**, 496 (2021).
[16] P. Behera *et al.*, Electric field control of chirality, Sci. Adv. **8**, eabj8030 (2022).
[17] A. Sawada, Y. Ishibashi, and Y. Takagi, Ferroelasticity and the origin of optical activity of $Ca_2Sr(C_2H_5CO_2)_6$ (DSP), J. Phys. Soc. Jpn. **43**, 195 (1977).
[18] H. Zabrodsky and D. Avnir, Continuous symmetry measures. 4. Chirality, J. Am. Chem. Soc. **117**, 462 (1995).
[19] S. Keinan and D. Avnir, Quantitative chirality in structure-activity correlations. Shape recognition by trypsin, by the D_2 dopamine receptor, and by cholinesterases, J. Am. Chem. Soc. **120**, 6152 (1998).
[20] D. Gao, S. Schefzick, and K. B. Lipkowitz, Relationship between chirality content and stereoinduction: Identification of a chiraphore, J. Am. Chem. Soc. **121**, 9481 (1999).
[21] M.-L. Du, F.-K. Guo, C. Hanhart, B. Kubis, and U.-G. Meißner, Where is the lightest charmed scalar meson? Phys. Rev. Lett. **126**, 192001 (2021).
[22] K. Kimura, M. Sera, and T. Kimura, A^{2+} cation control of chiral domain formation in $A(TiO)Cu_4(PO_4)_4$ (A = Ba, Sr), Inorg. Chem. **55**, 1002 (2016).
[23] S. Mühlbauer, F. Jonietz, C. Pfleiderer, A. Rosch, A. Neubauer, R. Georgii, and P. Böni, Skyrmion lattice in a chiral magnet, Science **323**, 915 (2009).
[24] H. Zhang, C.-X. Liu, and S.-C. Zhang, Spin-orbital texture in topological insulators, Phys. Rev. Lett. **111**, 066801 (2013).
[25] P. Shafer, P. García-Fernández, P. Aguado-Puente, A. R. Damodaran, A. K. Yadav, C. T. Nelson, S.-L. Hsu, J. C. Wojdeł, J. Íñiguez, L. W. Martin, E. Arenholz, J. Junquera, and R. Ramesh, Emergent chirality in the electric polarization texture of titanate superlattices, Proc. Natl. Acad. Sci. USA **115**, 915 (2018).
[26] Č. Koňák, V. Kopský, and F. Smutný, Gyrotropic phase transitions, J. Phys. C Solid State Phys. **11**, 2493 (1978).
[27] S. Hirotsu, Some optical and thermal properties of $CsCuCl_3$ and its phase transition near 423K, J. Phys. C Solid State Phys. **8**, L12 (1975).
[28] S. Hirotsu, Jahn-Teller induced phase transition in $CsCuCl_3$: Structural phase transition with helical atomic displacements, J. Phys. C Solid State Phys. **10**, 967 (1977).
[29] Y. Kousaka, H. Ohsumi, T. Komesu, T. Arima, M. Takata, S. Sakai, M. Akita, K. Inoue, T. Yokobori, Y. Nakao, E. Kaya, and J. Akimitsu, Crystallographic chirality of $CsCuCl_3$ probed by resonant circularly-polarized hard X-ray diffraction, J. Phys. Soc. Jpn. **78**, 123601 (2009).
[30] H. Ueda, E. Skoropata, M. Burian, V. Ukleev, G. S. Perren, L. Leroy, J. Zaccaro, and U. Staub, Conical spin order with chiral quadrupole helix in $CsCuCl_3$, Phys. Rev. B **105**, 144408 (2022).
[31] M. Nespolo, A note about the notion of chirality, Cryst. Res. Technol. **50**, 413 (2015).
[32] Y. Tanaka, T. Takeuchi, S. W. Lovesey, K. S. Knight, A. Chainani, Y. Takata, M. Oura, Y. Senba, H. Ohashi, and S. Shin, Right handed or left handed? Forbidden X-ray diffraction reveals chirality, Phys. Rev. Lett. **100**, 145502 (2008).
[33] H. Ueda, Y. Joly, and U. Staub, Non-chiral 1*T*-$TiSe_2$ creates circular dichroism in resonant X-ray diffraction via multipole scattering interference, Phys. Rev. B **111**, L081114 (2025).
[34] M. Aamir, M. Sher, M. A. Malik, J. Akhtar, and N. Revaprasadu, A chemodosimetric approach for the selective detection of Pb^{2+} ions using a cesium based perovskite, New J. Chem. **40**, 9719 (2016).
[35] A. M. Jafar, K. A. Khalaph, and A. M. Hmood, Lead-free perovskite and double perovskite solar cells, IOP Conf. Ser.: Mater. Sci. Eng. **765**, 012047 (2020).
[36] H. Ohsumi, A. Tokuda, S. Takeshita, M. Takata, M. Suzuki, N. Kawamura, Y. Kousaka, J. Akimitsu, and T. Arima, Three-dimensional near surface imaging of chirality domains with circularly polarized X-rays, Angew. Chem. Int. Ed. **52**, 8718 (2013).
[37] J. Petzelt, I. Gregora, V. Vorlíček, J. Fousek, B. Březina, G. V. Kozlov, and A. A. Volkov, Far-infrared and Raman spectroscopy of the phase transition in $CsCuCl_3$, J. Raman Spectrosc. **10**, 187 (1981).
[38] G. H. Fecher, J. Kübler, and C. Felser, Chirality in the solid state: Chiral crystal structures in chiral and achiral space groups, Materials **15**, 5812 (2022).
[39] C. P. Romao and D. M. Juraschek, Phonon-induced geometric chirality, ACS Nano **18**, 29550 (2024).
[40] Z. Zeng, M. Först, M. Fechner, M. Buzzi, E. Amuah, C. Putzke, P. J. W. Moll, D. Prabhakaran, P. Radaelli, and A. Cavalleri,

Photo-induced chirality in a nonchiral crystal, Science **387**, 431 (2025).

[41] L. Chaix, S. de Brion, F. Lévy-Bertrand, V. Simonet, R. Ballou, B. Canals, P. Lejay, J. B. Brubach, G. Creff, F. Willaert, P. Roy, and A. Cano, THz magnetoelectric atomic rotations in the chiral compound $Ba_3NbFe_3Si_2O_{14}$, Phys. Rev. Lett. **110**, 157208 (2013).

[42] S. Skiadopoulou, F. Borodavka, C. Kadlec, F. Kadlec, M. Retuerto, Z. Deng, M. Greenblatt, and S. Kamba, Magnetoelectric excitations in multiferroic Ni_3TeO_6, Phys. Rev. B **95**, 184435 (2017).

[43] M. Fava, E. McCabe, A. H. Romero, and E. Bousquet, A phonon-driven mechanism for an emergent and reversible chirality in crystals, arXiv:2405.12696.

[44] H. Ueda, A. Nag, C. P. Romao, M. García-Fernández, K. Zhou, and U. Staub, Chiral phonons in polar $LiNbO_3$, arXiv:2504.03330.

[45] PSI data repository, https://doi.psi.ch/detail/10.16907%2F89c49d98-784e-4f30-983b-67755c23a0b2.

[46] M. Suzuki, Y. Inubushi, M. Yabashi, and T. Ishikawa, Polarization control of an X-ray free-electron laser with a diamond phase retarder, J. Synchrotron Rad. **21**, 466 (2014).

[47] Z. Yang, L. Mutter, M. Stillhart, B. Ruiz, S. Aravazhi, M. Jazbinsek, A. Schneider, V. Gramlich, and P. Günter, Large-size bulk and thin-film stilbazolium-salt single crystals for nonlinear optics and THz generation, Adv. Mater. **17**, 2018 (2007).

[48] T. Nagao and J. Igarashi, Resonant x-ray scattering spectra from multipole ordering: Np $M_{4,5}$ edges in NpO_2, Phys. Rev. B **72**, 174421 (2005).

[49] A. W. Schlueter, R. A. Jacobson, and R. E. Rundle, A redetermination of the crystal structure of $CsCuCl_3$, Inorg. Chem. **5**, 277 (1966).

[50] F. D. J. Brunner, O.-P. Kwon, S.-J. Kwon, M. Jazbinšek, A. Schneider, and P. Günter, A hydrogen-bonded organic nonlinear optical crystal for high-efficiency terahertz generation and detection, Opt. Express **16**, 16496 (2008).

[51] X. Gonze, B. Amadon, G. Antonius, F. Arnardi, L. Baguet, J.-M. Beuken, J. Bieder, F. Bottin, J. Bouchet, E. Bousquet *et al.*, The ABINITproject: Impact, environment and recent developments, Comput. Phys. Commun. **248**, 107042 (2020).

[52] H. J. Monkhorst and J. D. Pack, Special points for Brillouin-zone integrations, Phys. Rev. B **13**, 5188 (1976).

[53] https://henriquemiranda.github.io/phononwebsite/index.html.